Cell Reports
Physical Science

Article

Phase segregation dynamics in mixed-halide perovskites revealed by plunge-freeze cryo-electron microscopy

Graphical abstract

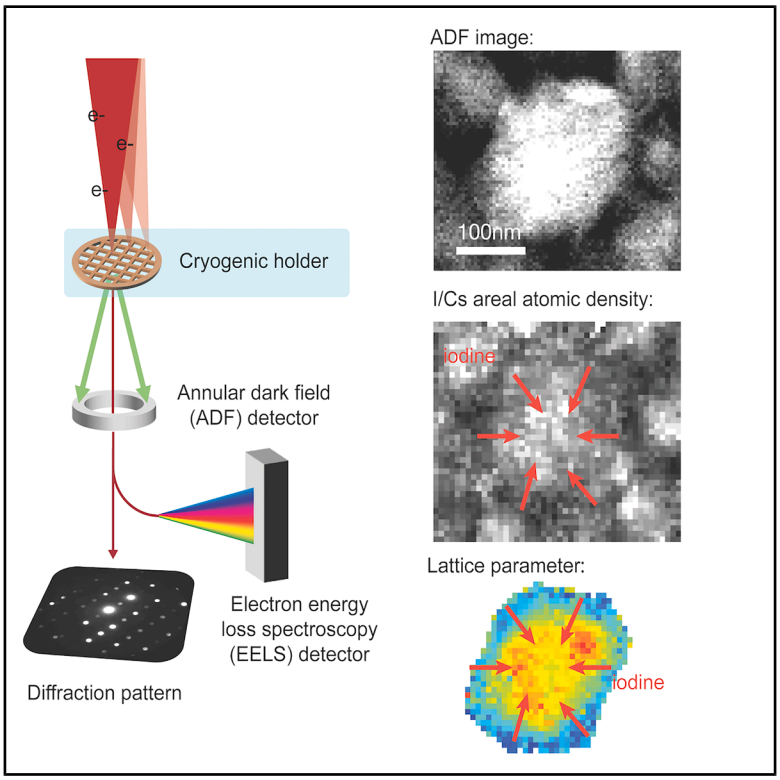

Highlights

- Cryoelectron microscopy captures transient ion distributions in the perovskites
- Capturing intermediate states during light-induced segregation in the halide perovskites
- Plunge-freeze plus 4D-STEM enable visualization of halide segregation dynamics

Authors

Qingyuan Fan, Yi Cui, Yanbin Li, ..., Yi Cui, Hemamala I. Karunadasa, Aaron M. Lindenberg

Correspondence

yicui@stanford.edu (Y.C.), hemamala@stanford.edu (H.I.K.), aaronl@stanford.edu (A.M.L.)

In brief

Fan et al. employ a plunge-freeze technique combined with cryoelectron microscopy to capture transient ion distributions during light-induced phase segregation. The approach offers a new view of the intermediate states and reversible nature of light-induced phase segregation in mixed-halide perovskites.

Fan et al., 2025, Cell Reports Physical Science 6, 102653
June 18, 2025
https://doi.org/10.1016/j.xcrp.2025.102653

CellPress

Cell Reports
Physical Science

CellPress
OPEN ACCESS

Article

Phase segregation dynamics in mixed-halide perovskites revealed by plunge-freeze cryo-electron microscopy

Qingyuan Fan,[1,2,3,10] Yi Cui,[1,10] Yanbin Li,[1,10] Julian A. Vigil,[4,5,10] Zhiqiao Jiang,[1,4] Partha Nandi,[6] Robert Colby,[7] Chensong Zhang,[8] Yi Cui,[1,2,9,*] Hemamala I. Karunadasa,[2,4,*] and Aaron M. Lindenberg[1,2,3,11,*]

[1]Department of Materials Science and Engineering, Stanford University, Stanford, CA 94305, USA
[2]Stanford Institute for Materials and Energy Sciences (SIMES), SLAC National Accelerator Laboratory, Menlo Park, CA 94025, USA
[3]Stanford PULSE Institute, SLAC National Accelerator Laboratory, Menlo Park, CA 94025, USA
[4]Department of Chemistry, Stanford University, Stanford, CA 94305, USA
[5]Department of Chemical Engineering, Stanford University, Stanford, CA 94305, USA
[6]ExxonMobil Technology and Engineering Company, BTEC-W, 5200 Bayway Drive, Baytown, TX 77520, USA
[7]ExxonMobil Technology and Engineering Company, Annandale, NJ 08801, USA
[8]Department of Molecular and Cellular Physiology, Stanford University, Stanford, CA 94305, USA
[9]Department of Energy Science and Engineering, Stanford University, Stanford, CA 94305, USA
[10]These authors contributed equally
[11]Lead contact
*Correspondence: yicui@stanford.edu (Y.C.), hemamala@stanford.edu (H.I.K.), aaronl@stanford.edu (A.M.L.)
https://doi.org/10.1016/j.xcrp.2025.102653

SUMMARY

Mixed-halide lead perovskites, with photoexcited charge-carrier properties suitable for high-efficiency photovoltaics, hold significant promise for high-efficiency tandem solar cells. However, phase segregation under illumination, where an iodide-rich phase forms carrier trap states, remains a barrier to application. This study employs plunge-freeze cryoelectron microscopy to visualize nanoscale phase segregation dynamics in $CsPb(Br_xI_{1-x})_3$ films. By rapidly freezing the illuminated samples, we preserve transient photoexcited ion distributions for high-resolution structural and compositional analysis at the nanoscale. Cryogenic scanning transmission electron microscopy (STEM) techniques (electron energy loss spectroscopy [EELS] and 4D-STEM) captured the dynamics of photo-induced iodine migration from grain boundaries to centers, identified the buildup of anisotropic strain, and captured the heterogeneous evolution of this process within a single grain. These findings provide insight into microscopic phase segregation mechanisms and their dynamics, enhancing our understanding of mixed-halide perovskite photostability.

INTRODUCTION

Halide perovskites have garnered interest in the field of optoelectronics due to the ease of large-area, low-cost film preparation methods and their high photoluminescence (PL) and photovoltaic conversion efficiency.[1–4] With a common chemical formula of ABX_3, various A-site cations (e.g., Cs^+, $CH_3NH_3^+$ (MA^+), and $CH(NH_2)_2^+$ (FA^+)) and X-site anions (e.g., I^-, Br^-, and Cl^-) have been widely investigated in perovskites with Pb^{2+} as the B-site cation. Among these materials, mixed-halide perovskites are particularly suitable for building tandem solar cells[5] since the band gap is tunable from UV to near-infrared by varying the X-site (halide) composition.[6–8] However, photoinstability, manifesting as demixing of the halides under illumination, remains an important obstacle to their application in photovoltaic and light-emitting devices.[9,10] The photo-induced formation of iodide-rich domains induces undesired band-gap decreases, which results in decreased open-circuit voltages and reduced device-level performance.[8,11]

Nearly a decade has passed since Hoke et al. first reported the observation of phase segregation in $(CH_3NH_3)Pb(Br_xI_{1-x})_3$,[12] but the fundamental microscopic mechanisms underlying this behavior, and even basic aspects of how the local stoichiometry changes, remain controversial and widely debated.[10] Bulk characterization methods, such as PL and X-ray diffraction (XRD),[12] were first employed to verify and study the extent of phase segregation. Upon visible-light illumination, the red-shifted PL emission and split XRD peaks indicated the formation of phases with distinct halide ratios.[12,13] Various mechanisms have been proposed, typically involving non-equilibrium dynamical effects, to explain the initiation and evolution of ion migration. For example, the proposed driving forces for phase segregation include the temperature-dependent miscibility gap,[14] the release of polaronic strain through the formation of I-rich domains,[15] carrier funneling toward lower-band-gap I-rich regions,[16,17] and defects, especially near grain boundaries.[18]

Spatially resolved optical probes, such as confocal PL,[13,18–20] cathodoluminescence,[15] and X-ray fluorescence,[21] have been

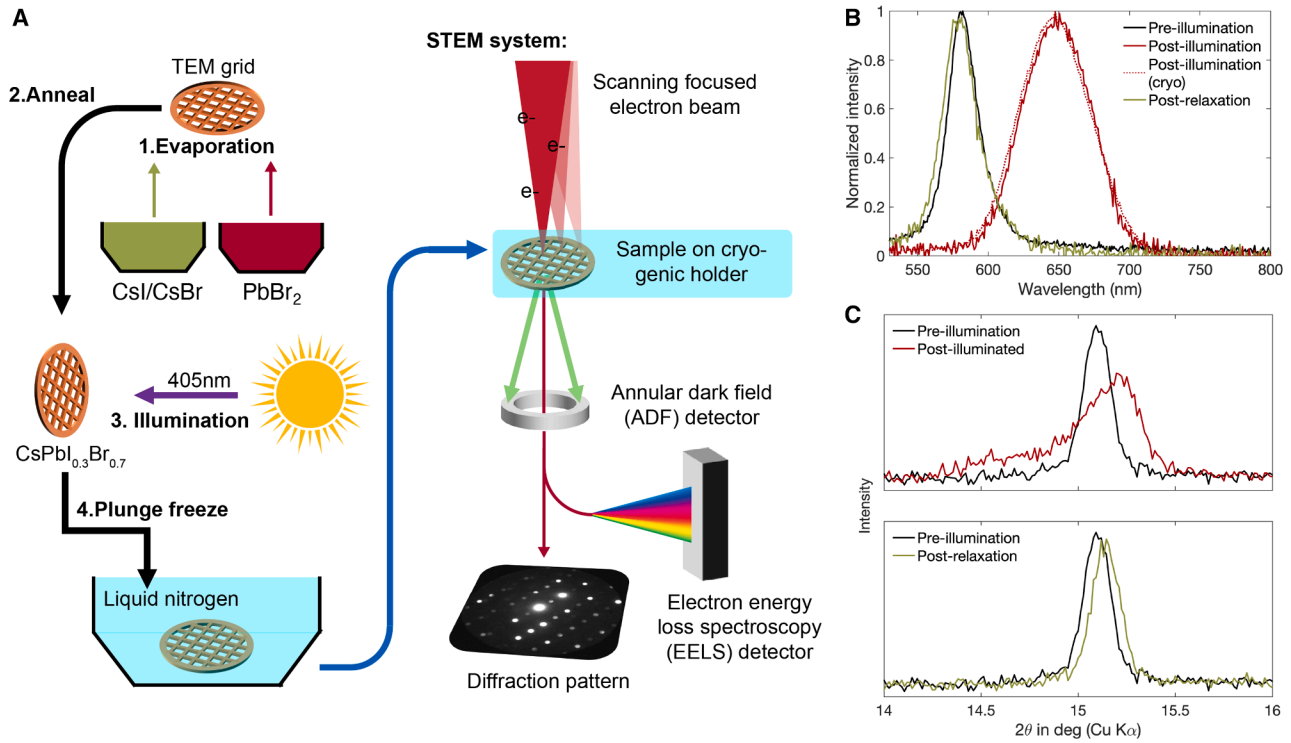

Figure 1. Characterization approach for capturing phase segregation

(A) Schematic diagram of the sequential sample preparation, plunge-freeze approach, and coupled cryoelectron microscopy approach reported here.

(B and C) Photoluminescence emission spectra (excitation wavelength = 405 nm) (B) and thin-film XRD patterns measured in the region of the (100) pseudo-cubic Bragg reflection (C), including for pristine $CsPb(Br_{0.7}I_{0.3})_3$ (pre-illumination), post-illumination, post-illumination (cryo) stored for 3 weeks, and post-relaxation (see the main text for a description of each condition).

employed to identify regions with different halide compositions.[12] Kelvin probe force microscopy has revealed the contact surface potential, with sensitivity to ion migration at grain boundaries.[22] To achieve more direct elemental characterization, techniques such as energy-dispersive X-ray spectroscopy (EDX or EDS)[17] and electron energy loss spectroscopy (EELS) offer detailed information on the spatial distribution of I-rich and Br-rich regions. The majority of studies state that the distributions of I-rich and Br-rich phases are influenced by morphology, with many specifically indicating that I-rich phases tend to form near grain boundaries and sample edges.[12,18,19] However, there are also reports of I-rich and Br-rich phases forming across grain boundaries or I-rich domains appearing in the grain centers, away from grain boundaries, or in single crystals.[23,24] These contradictory findings highlight the need for *in situ* microscopic studies and high-resolution analysis of defects and strain states as the phase segregation process occurs.

A central challenge in elucidating the mechanisms for photodegradation arises from the intrinsically dynamical nature of these processes. Phase segregation is reversible over minutes to hours without illumination, and measurements that average in space or time essentially blur the atomic to mesoscale processes that are occurring. Prior spatially resolved methods have not been able to provide an *in situ* view of this process or to track the underlying intrinsically dynamical ion motions under device-relevant conditions. Scanning-based PL and cathodoluminescence (CL) measurements usually take minutes or longer to complete, especially when the spatial resolution is high. As a result, these techniques are usually applied after illumination or at equilibrium under continuous illumination without the ability to capture the transient moments of the segregation process.[17] Further, optical probe methods often provide only indirect measurements, relying on local band-gap variations in the material. Due to the carrier funneling effect[13,25] and the resulting significantly higher PL efficiency in I-rich domains, PL imaging typically highlights regions with the highest iodide composition, potentially overlooking areas where iodide is not predominant. Similarly, cathodoluminescence measurements are operated under electron irradiation in vacuum and provide indirect measurements based on the optical properties of the material. Therefore, characterization approaches that offer high spatial resolution while simultaneously capturing the transient ion distribution and its evolution are crucial to understanding the photodegradation mechanisms.

Here, we apply an approach that enables the tracking of the transient ion distribution and nanoscale structural changes induced by illumination at room temperature. This method utilizes a plunge-freeze technique[26] (Figure 1), where photoexcitation at room temperature under normal atmospheric conditions triggers the segregation process, which then develops over a programmable time period. The samples are then rapidly plunged into liquid nitrogen, effectively freezing the transient

configuration, which is then analyzed using cryoelectron microscopy (cryo-EM) techniques (details are included in Figure S1). The cryogenic conditions also address the issue of mixed-halide perovskites' sensitivity to electron doses at room temperature.[26,27]

RESULTS

Experimental approach

Here, we prepared $CsPb(Br_xI_{1-x})_3$ perovskite films with thicknesses of ca. 100 nm by sequential thermal evaporation of CsI/CsBr and $PbBr_2$ directly on carbon film-Cu transmission electron microscopy (TEM) grids, followed by annealing under N_2 atmosphere (see supplemental information for experimental methods). PL emission and XRD measurements, averaged over the entire sample, are conducted to verify the band gap and pseudo-cubic perovskite structure, respectively, of the pristine polycrystalline film. To trigger photo-induced phase segregation at room temperature, the sample was illuminated under N_2 atmosphere using a 405-nm light-emitting diode (LED) with an intensity of 0.4 W/cm^2. The illumination is conducted within the plunge-freeze setup (Figure 1A) to freeze the sample once a desired time of illumination is reached, allowing for subsequent characterization of the frozen-in structure. We note that symmetry-lowering solid-solid phase transitions are well known in the perovskites upon cooling from high temperature[28]; however, rapid freezing helps prevent phase transitions that might occur under slower, equilibrium cooling. Particular to this work, the equilibrium phase diagram for $CsPb(Br_xI_{1-x})_3$ has primarily been investigated at high temperatures (e.g., 330°C, where the phase is cubic for all x)[29]; at room temperature, most compositions within $CsPb(Br_xI_{1-x})_3$ appear stable as a polycrystalline film,[30] though the descent in symmetry from the high-temperature cubic phase differs with x, growth and annealing conditions and the substrate. Thus, we report all Bragg reflections with (pseudo-)cubic Miller indices for consistency without a discernable tetragonal or orthorhombic distortion, which indicates the absence of phase changes during the plunge-freeze operations.

PL and XRD characterization

The PL emission spectrum was first measured following various illumination times, ranging from 0 to 8 min. Prior to illumination, the PL peak at 580 nm (Figure 1B, pre-illumination) indicates a halide composition ratio of I/Br = 0.45, derived by comparing the PL spectrum with those of previously studied perovskites with varying halide compositions.[31] EELS characterization, discussed later, illustrates that the composition is $CsPb(Br_{0.7}I_{0.3})_3$. Upon illumination, the PL peak redshifts, and the intensity increase begins to saturate at 5 min, indicating that the phase segregation process is fully achieved after 5 min of illumination (Figure S8). After illumination for 5 min, the PL peak redshifts to 651 nm (Figure 1B, post-illumination), matching the PL wavelength of $CsPb(Br_{0.27}I_{0.73})_3$[32] and indicating the formation of a lower-band-gap I-rich phase. The same measurement is applied to the sample illuminated for 5 min, followed by 2 h of resting in a dark environment. The post-relaxation PL spectrum (Figure 1B) shows a peak wavelength of 579 nm, which demonstrates the reversibility of the photo-induced phase segregation. A small blueshift is likely due to partial iodide loss under illumination, as the lower iodide ratio corresponds to a smaller PL emission wavelength.

On the same samples, XRD results provide structural information that corroborates the PL data. The thin-film XRD pattern shows strong (h00) pseudo-cubic Bragg reflections from the pristine $CsPb(Br_{0.7}I_{0.3})_3$ structure (Figure S5), with a corresponding pseudo-cubic lattice parameter of ca. 5.87 Å. In Figure 1C (top), the (100) Bragg peak exhibits broadening after illumination, indicating a wider lattice-parameter distribution concomitant with phase segregation. The similarity of the XRD patterns following relaxation (compared to the pristine film) also demonstrates reversibility in the average structure, albeit with a small, irreversible lattice-parameter decrease, again likely arising from iodide loss.

To carry out high-resolution cryogenic characterization, photoexcited samples are subsequently plunge frozen at T = 77 K. For post-illumination samples, the PL spectrum measured after 3 weeks of storage in liquid nitrogen (Figure 1B, red dashed curve) is in good agreement with that obtained at room temperature (Figure 1B, red solid curve), indicating that cryogenic conditions inhibit reversible ion migration while preserving the crystal structure and frozen-in, transient ion distribution. Subsequent characterization employing 4D-scanning TEM (STEM) conclusively demonstrates the effective preservation of crystalline architecture achieved via the freezing protocol. As a result, the plunge-freeze approach thus provides access to the intrinsic, instantaneous configuration of the photoexcited, phase-segregated samples.

Cryo-STEM measurements

To explore the phase segregation process further, three cryo-STEM-based techniques—annular dark-field (ADF) imaging, EELS, and 4D-STEM—are employed to analyze the same sample areas, providing insights into morphology, stoichiometry, and structure, respectively. The ADF images reveal variations in grain size ranging from 100 to 400 nm (Figure 2A).

In this study, EELS provides areal atomic density data for the elements. The EELS spectrum (Figure 2B), particularly the M_5 peak for I and the M_4 peak for Cs, is used to calculate the areal atomic density of these elements for each pixel across the imaging area. The examples of areal atomic density mapping of I and Cs are shown in Figures S2 and S3. Since the EELS detector's range does not encompass the energy of Br peaks, a direct calculation of the ratio between I and Br is not feasible. The atomic areal densities of iodine are influenced by the sample thickness, which is smaller at the grain boundary. Since the focus is on the stoichiometric composition of halide elements rather than areal atomic density, it is necessary to remove the influence of sample thickness to accurately represent the halide ratio distribution. Diffraction patterns (Figures 2D and S8) confirm that the perovskite structure remains unchanged, suggesting that the volume atomic density of Cs^+ is constant. Therefore, the areal density of cesium is proportional to the sample thickness. By calculating the areal atomic density ratio of iodine to cesium (I/Cs) within the perovskite, the halide composition can be accurately determined (Figures S2D and S3D). This I/Cs ratio is mapped with a resolution of 10 nm and displayed in Figure 2C, corresponding to the transient elemental

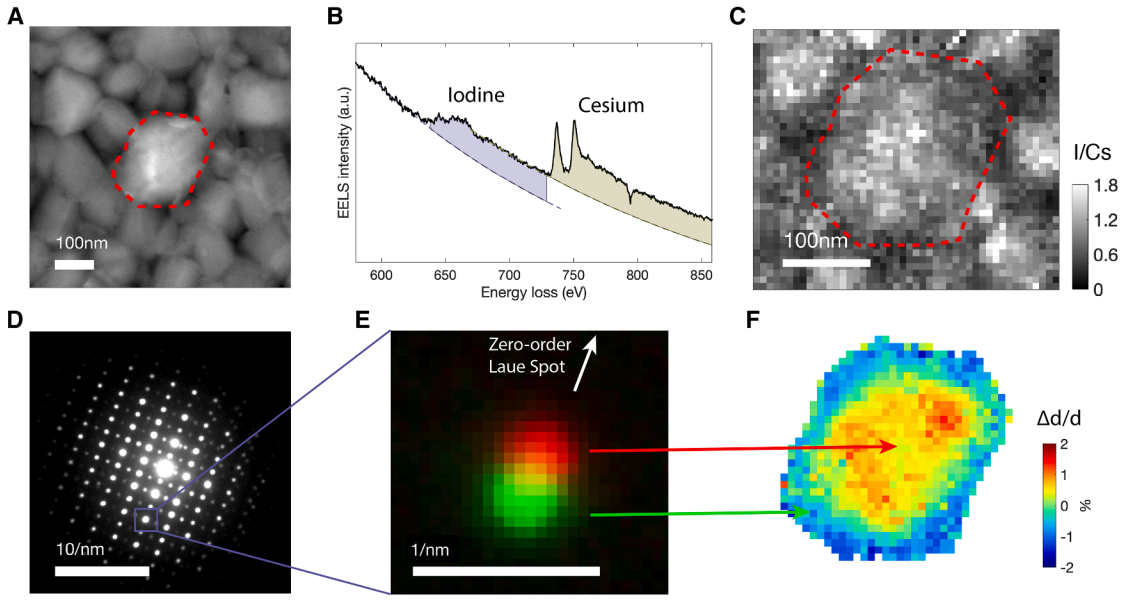

Figure 2. Morphology, stoichiometry, and structural imaging of the photoexcited mixed-halide perovskite

(A) Annular dark-field (ADF) image of the polycrystalline sample. The grain in the center, outlined by the red dashed line, indicates the area analyzed in subsequent EELS (C) and 4D-STEM (F) results.

(B) Representative EELS spectrum of an area on the grain. The color filling indicates the integration area for calculating the areal atomic density of iodine (blue) and cesium (green).

(C) Mapping of the I/Cs ratio (integrated counts) over the area for frozen configuration at t = 5-min illumination. Each pixel includes calculation as shown in (B).

(D) Selected area diffraction pattern of a 40 × 40 nm area in the grain center.

(E) The diffraction peaks (red: in the grain center, green: near grain boundary) zoomed in to the purple square in (D).

(F) Map of the percentage of lattice-parameter change (Δd/d) at t = 5-min illumination. The value for each pixel is calculated from the diffraction pattern, averaging over several diffraction peaks. The pixel size is 10 × 10 nm.

configuration after photoexcitation for t = 5 min (discussed further below).

4D-STEM provides complementary high-resolution local structural information.[33] Utilizing the STEM mode of a cryogenic microscope, a focused electron beam with a small divergence angle generates a 2D diffraction pattern at each detected sample position. By scanning the electron beam across the sample surface, detailed structural information is obtained. This technique not only reveals crystal symmetry and orientation but also enables quantitative analysis of the average lattice parameter via reciprocal-space mapping. In this study, diffraction patterns and quantitative analyses are performed at each pixel within the scanned area, with a pixel resolution of 10 nm.

The single-crystal diffraction patterns obtained from the 4D-STEM results (an example is shown in Figure 2D) confirm that the crystal remains in the (pseudo-)cubic perovskite phase during the cooling process (Figure S6), consistent with the structural determined by XRD measurements at room temperature (Figure S5). The lattice parameter of 5.80 Å at T = 77 K shows close agreement with the room temperature value of 5.87 Å, as previously mentioned. The minor discrepancy between these values may be attributed to slight variations in halide composition among the measured samples and contributions from thermal expansion. Furthermore, diffraction patterns taken at various positions within a grain confirm that I-rich and Br-rich domains within the same grains maintain a continuous crystal structure, sharing the same space-group symmetry and local orientation.

The dynamical segregation process is studied by applying the EELS and 4D-STEM methods on the pre-illumination, post-illumination (t = 5 min) (corresponding to frozen in structure), and post-relaxation samples. The I/Cs ratio mapping shows uniform halide mixing in the pristine $CsPb(Br_{0.7}I_{0.3})_3$ perovskite samples (Figure 3A). Post-illumination analysis shows distinct contrasts in the I/Cs ratio, with a higher iodine concentration at the grain center and lower concentrations near the grain boundaries, as revealed by correlating EELS mapping with ADF imaging (Figure 3B). The EELS results from the post-relaxation samples (Figure 3C) also demonstrate uniform iodine distribution, confirming the reversible nature of the phase segregation process. We note that a comparison of the pre-illuminated to post-illuminated 4D-STEM and EELS results shows that no phase segregation is induced by electron beam irradiation. Results on more samples under identical conditions for the pre-illumination, post-illumination, and post-relaxation cases are shown in Figure S8, demonstrating the same dynamic segregation process.

After illumination in the frozen-in configuration, the averaged I/Cs ratio in the central part of the grains (I/Cs = 1.19) exceeds the averaged value in the pristine samples (I/Cs = 0.88), indicating iodine ion migration from near the grain boundaries toward the centers (schematically shown in Figure 3D). The

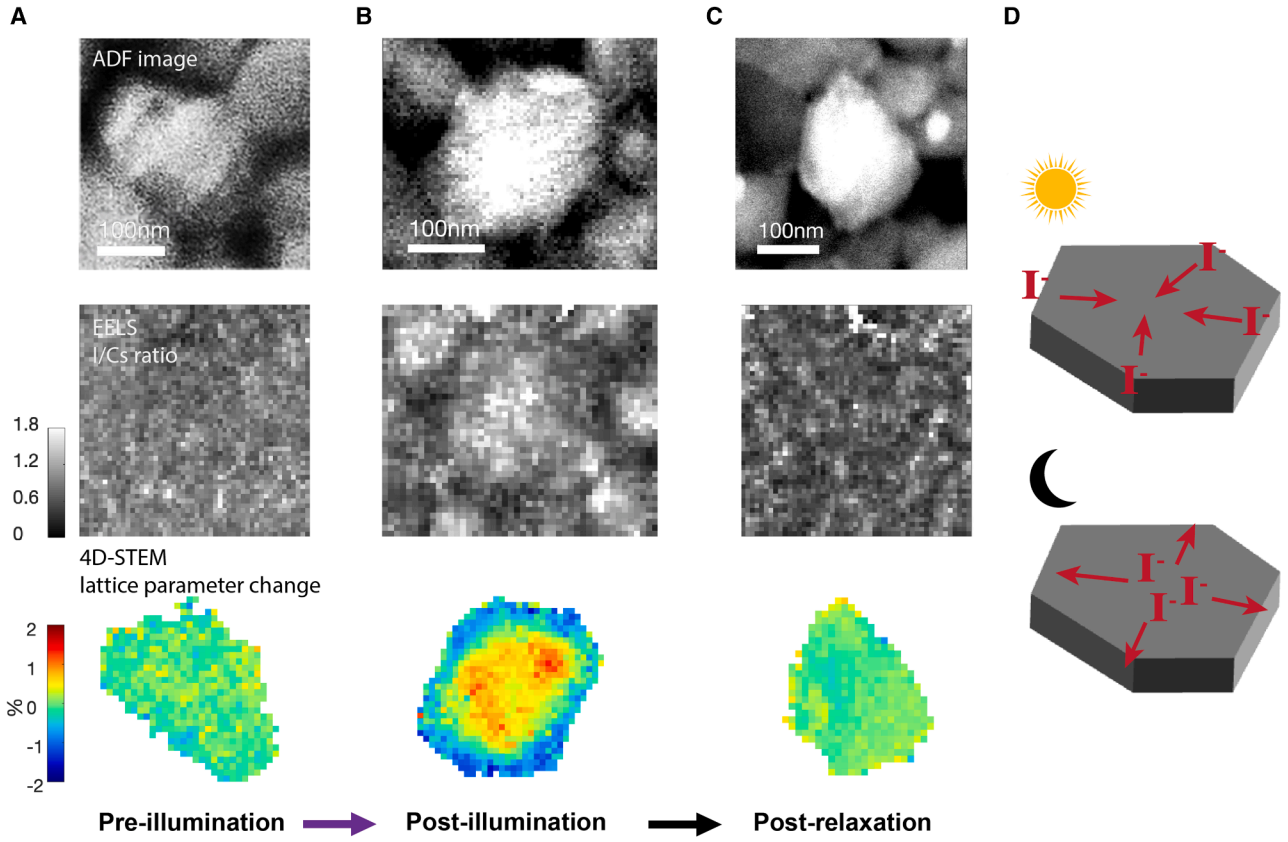

Figure 3. Correlated morphology, stoichiometry, and structural imaging for the pristine, illuminated, and relaxed, self-healed mixed-halide perovskite

(A–C) ADF image (top), I/Cs ratio from EELS mapping (middle), and percentage of lattice-parameter change from 4D-STEM (bottom) for (A) pre-illumination, (B) post-illumination (t = 5 min), and (C) post-relaxation samples.

(D) Schematic diagram showing the apparent intragrain iodide migration directions while under illumination (top) and during dark relaxation (bottom).

All images in each column (ADF, EELS, and 4D-STEM) share the same scale bar.

distribution of measured I/Cs ratios in the region within 30 nm of the grain boundary (blue) and that in the grain center (red) are shown by the histograms in Figure 4. In addition to the differences in the average halide composition between these regions, Figure 4 (middle) highlights the heterogeneity of the I/Cs ratio, revealing a wide distribution at both the grain boundary and grain center. We note that an average I/Cs ratio of 1.19 is expected to produce significantly smaller PL shifts, corresponding to emission at approximately 605 nm,[31] which contrasts with the shift to 651 nm observed experimentally (Figure 1B). This discrepancy can be attributed to the long tails in the distribution of the I/Cs ratio, extending up to 1.8 (Figure 4, middle top). These tails indicate that regions with high I/Cs ratios, though only a small fraction of the sample, exert a disproportionate influence on the PL shifts. This occurs because excited carriers tend to funnel into these regions with the lowest band gap, thereby amplifying the observed PL shifts.[9,12,25]

4D-STEM measurements of the plunge-frozen samples are correlated with ADF and EELS mapping. Although regions within the same grain exhibit identical crystal symmetry and orientation, variations in lattice parameters are observed. In Figure 2E, diffraction peaks from different positions within a grain (red: center, green: near boundary) are plotted together for comparison under the same view box. The variation in peak position along the direction pointing to the zero-order diffraction spot indicates strain across the segregated grain area. The lattice parameter mapping (Figure 3) derived from 4D-STEM, averaged over multiple diffraction peaks, shows trends that align with the EELS results. The uniform lattice parameter distribution across the pre-illumination grain matches the uniform I/Cs ratio. In the post-illumination samples, the regions with a large lattice parameter are predominantly located at the grain centers, a pattern that is reversed when samples are rested in a dark environment. Considering that iodine atoms are larger than bromine atoms, perovskites with higher iodine content exhibit larger lattice parameters; thus, the results of the structural studies closely match the measurements on film stoichiometry. Additionally, the 4D-STEM results reveal no pre-existing strain within the detection limits before phase segregation, whereas the post-illumination strain distribution shows values of over 4%.

Figure 4 (bottom) illustrates the histograms of lattice parameter distribution, which are calculated by averaging the lattice

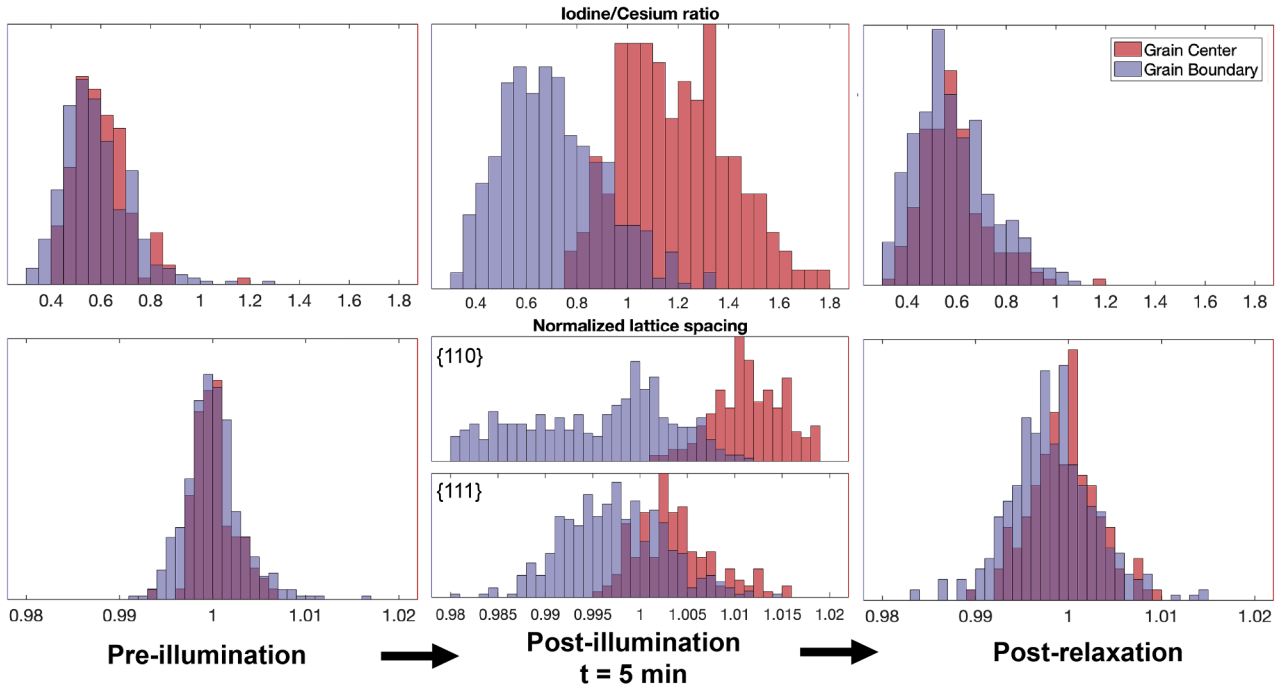

Figure 4. Histograms of the measured I/Cs ratio (EELS) and strain (4D-STEM) of various samples and areas

Histogram of the I/Cs ratio (top) and normalized lattice-parameter change (bottom) for pre-illumination, post-illumination, and post-relaxation samples. The blue histograms (grain boundary) count the data from any area less than 30 nm away from the grain boundary, indicating the near-boundary area. The red (grain center) histograms count the data from any area more than 30 nm away from the grain boundary. The lattice parameters for pre-illumination and post-relaxation samples are analyzed by averaging the lattice parameters corresponding to all diffraction peaks, while the lattice parameters are separated by two orthogonal families of planes ({110} and {111}) on the post-illumination samples to illustrate the anisotropic strain. Each histogram includes 160–250 data points of the scanned area.

parameters corresponding to multiple diffraction peaks. For the pre-illumination and post-relaxation samples without phase segregation, the lattice parameter distributions are narrow. The lattice parameters of the grain center (red) and grain boundary (blue) areas show a similar lattice with a narrow distribution, which corresponds with the uniform I/Cs stoichiometry. In contrast, the lattice parameter distributions of the post-illumination (5 min) films are broader, with different averaged values for grain center and grain boundary samples, which corresponds with the heterogeneous I/Cs ratio for the samples with segregation. Here, the lattice parameter distribution is analyzed separately for two orthogonal families of planes (top: {110}, bottom: {111}). The anisotropic strain will be discussed with the diffraction results subsequently.

To quantitatively characterize the morphology and time dependence of the I-rich domain distribution, the correlation coefficient between the ADF signal and the I/Cs ratio is calculated for various light exposure times (Figure 5A). The ADF signal is higher at the grain center and lower at the grain boundary, a distribution that correlates with the thickness difference in these regions. Thus, a positive correlation coefficient corresponds to a higher iodine composition at the grain center. The pristine sample, which has a uniform I/Cs ratio, yields coefficients close to zero, whereas the segregated samples exhibit positive correlation values that grow with cumulative illumination time. In particular, data from over 80 EELS and ADF mappings on samples with varying illumination times (Figure S7) reveal an increasing iodide concentration at the grain center. The correlation coefficients between the I/Cs ratio and ADF values show a gradual increase at the onset of segregation, with illumination times as short as 1 and 2 min. These correlation results suggest that the ion migration process is morphology dependent from the early stages of segregation, challenging the notion that I-rich clusters nucleate stochastically before migrating to specific regions of the grain (center/boundary).[23] The broadening of the correlation distribution with time, as shown by the error bars in Figure 5A, also indicates the key role of heterogeneity in this process, consistent with the histograms shown in Figure 4.

The 4D-STEM measurements additionally allow for analysis of the anisotropic nature of the phase segregation process within a single grain. Distinct from the maps shown in Figure 3C, the lattice parameter derived from two orthogonal families of planes ({110} and {111}) are mapped in Figures 5C and 5D, respectively, exhibiting significantly larger contrast in Figure 5C as compared to Figure 5D. This observation indicates segregation-induced anisotropy within grains, with the strain being larger along certain local crystallographic directions. The more quantitative analysis is demonstrated in the histograms in Figure 4 (bottom, middle), which show a larger lattice parameter contrast between grain center and near-boundary areas for {110} planes (Figure 5C), while the contrast is less pronounced in the {111} planes (Figure 5D), indicating anisotropic strain. A more comprehensive analysis of anisotropy, which includes a correlation coefficient mapping that tracks individual diffraction peaks, is presented

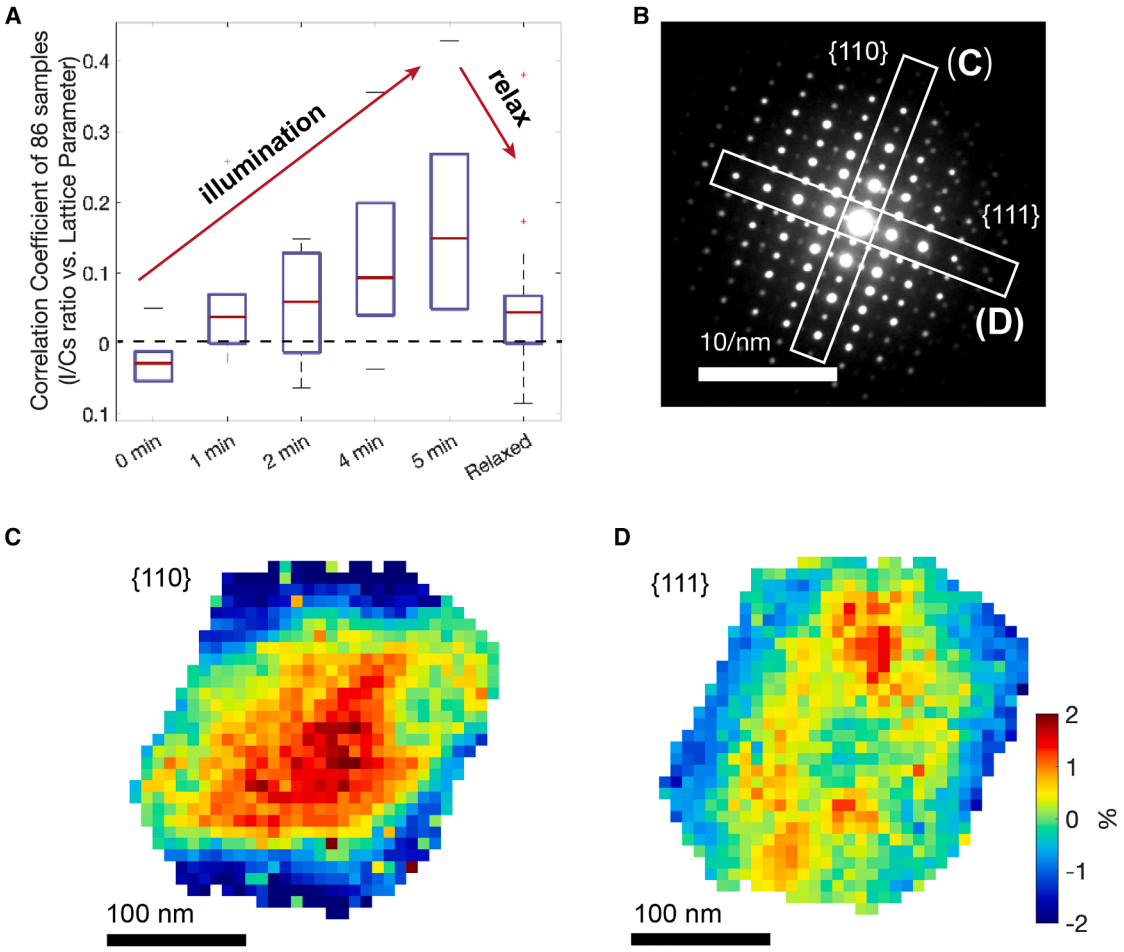

Figure 5. Evolution and anisotropy of the intragrain photo-induced phase segregation process

(A) Pearson product-moment correlation coefficients between ADF and EELS mapping (I/Cs ratio) with various illumination times and post-dark relaxation at the grain center. The statistical results are obtained from 86 samples. Central orange line: median, box limits: first quartile (Q1, 25%) and third quartile (Q3, 75%); whiskers extend to extreme data within 1.5× interquartile range (IQR); +, outliers.

(B–D) Selected area diffraction pattern (B). The percentage change in lattice parameter—calculated from diffraction families shown in (C) and (D)—are mapped using the same color palette.

in the supplemental information (Figure S4). The spatial distribution of the lattice parameter also suggests a directional lattice strain extending from the grain center to the boundary. This anisotropic strain may be determined by the grain morphology or other pre-existing strain or defect conditions. Understanding the anisotropy of the strain within individual grains is important for understanding the phase segregation mechanism, including the influence of initial morphology and defects. Notably, prior studies have identified the important role of strain in mediating the halide segregation process.[34]

DISCUSSION

Previous reports have documented various spatial distributions of I-rich regions during phase segregation, with contradictory results.[35,36] The majority of the literature supports the conclusion that phase segregation tends to occur near grain boundaries[15,17,20,22] or crystal edges,[13,18] though some also demonstrated boundary independence in large grain samples.[23] Specifically, many studies have argued that I-rich domains often form near these boundaries,[13,18] contrary to our findings. Others have observed that I-rich and Br-rich domains form across the boundaries.[17] Additionally, certain PL mapping studies have identified I-rich clusters or phases at the grain centers in all or some of the samples,[15,24] which contradicts previous results but is consistent with our measurements.

So far, it is not clear whether these findings represent an intrinsic and universal property of the phase segregation mechanism or if the microscopic details are strongly influenced by defect chemistry, substrates, grain size, strain, or fabrication method. The perovskite film thickness of 100 nm employed in this study is notably thinner compared to the typical thickness range of several hundred nanometers used in optoelectronic device applications. This reduced thickness was deliberately chosen to facilitate high-resolution TEM and STEM characterizations. However, such dimensional reduction may introduce distinct

morphological and defect characteristics that could influence phase segregation behavior. The increased surface-to-volume ratio in thinner films, analogous to near-boundary regions in thicker films, may potentially accelerate ion migration processes.

High-spatial-resolution characterization approaches, as presented here, hold promise to explore dependencies on spatial defects. Overall, this research indicates via direct measurements that dynamic iodine motion occurs toward the grain center under photoexcitation and identifies the heterogeneity in the phase segregation process. This research provides a window into phase segregation in mixed-halide perovskite films, specifically $CsPb(Br_{0.7}I_{0.3})_3$, using cryo-EM combined with a plunge-freeze technique, focusing on the spatial distribution of I-rich and Br-rich domains within the perovskite structure. The cryogenic approach effectively preserves the transient ion distributions, offering a view of the dynamics and reversible nature of light-induced phase segregation while maintaining the structural integrity of the material. The use of advanced electron microscopy techniques, including ADF, EELS, and 4D-STEM, provides high-resolution insights into the morphological, compositional, and structural details of the segregated phases. This research shows the time-dependent development of a higher concentration of iodine at the grain centers from element density mapping, supported by strain mapping. The usage of 4D-STEM also shows the anisotropic and heterogeneous strain after segregation. Future efforts could usefully be applied toward the investigation of a broad range of halide compositions, the associated temperature-dependent kinetics of these processes, and the further investigation of the anisotropic strain responses observed. The development of the plunge-freeze method also defines opportunities in the characterization of the dynamical properties of other materials undergoing light-induced structural transitions or other thermally activated processes.

METHODS

Sample preparation

Cesium lead halide perovskite ($CsPbX_3$; X = Br and I) thin films were grown on various substrates by sequential thermal evaporation and annealing. Substrate cleaning and preparation are described above; all manipulations following substrate preparation were carried out in N_2-filled gloveboxes. In typical thermal evaporation, two bare glass substrates and two glass-polydimethylsiloxane (PDMS)-grid stacks were mounted near the center of a mask holder. The holder was then transferred into the main chamber of a custom thermal evaporator (Thermionics VE-90 vacuum system controller; Inficon XTM/2 deposition monitor) within the same glovebox. In this geometry, the exposed side of each substrate faces the source—heated by electrical contact through the floor of the glovebox—which is initially obscured by a manual shutter. Next, polycrystalline powders of the source compound(s) were mounted on a flat tantalum boat (Kurt J. Lesker) and connected to the electrical leads. A top-mounted steel bell jar was slowly lowered to secure the chamber before engaging the vacuum pumps. The pressure was reduced to ca. 5×10^{-6} Torr or lower before the source was heated.

The thermal evaporation was carried out sequentially in two steps owing to the disparity in the melting points and vapor pressures of the source halide salts. We adapted the compositions and thickness ratios of the precursors from conditions within a prior report.[34] Indeed, the deposition rate and total thickness values reported by the quartz deposition monitor are estimates absent rigorous calibration; we used average density values for mixtures and reported impedance Z-factors when available. In a typical deposition of $CsPb(Br_{0.7}I_{0.3})_3$ (see the main text), a 3:1 mixture of CsI:CsBr (weight) was first evaporated with an applied current of ca. 8.5 A, resulting in a deposition rate of 0.5–3 Å s^{-1}, to a thickness of 480 Å (48.0 nm). After changing the source, $PbBr_2$ was evaporated with an applied current of ca. 6.5 A, resulting in a deposition rate of 1–2 Å s^{-1}, to a thickness of 515 Å (51.5 nm). These bilayer precursor films were subsequently transferred to another N_2-filled glovebox under N_2 or reduced pressure.

Bilayer precursor films on glass were annealed by direct back contact on a hot plate, whereas TEM grids were removed from the PDMS stack and transferred to an aluminum grid-heating block (Pelco; Ted Pella) on top of the hot plate. Annealing conditions were optimized by evaluating the crystal structure and PL emission of films deposited on glass substrates. We found that a rapid rise time and slow cooling led to the optimal phase purity, grain size, and PL yield from the resulting mixed-halide perovskite, $CsPb(Br_{0.7}I_{0.3})_3$. Specifically, precursor films on glass and the grid block were transferred to a hot plate stabilized at 170°C for 15 min before turning off the hot plate to allow slow cooling to room temperature. The resulting $CsPb(Br_{0.7}I_{0.3})_3$ thin films were stored under N_2 prior to illumination or measurement.

For substrate preparation, square borosilicate glass substrates (thickness: 1 mm) were scrubbed with detergent and subsequently sonicated in detergent, de-ionized water, acetone, and isopropanol (10 min each). The substrates were dried under N_2 flow and immediately used to mount TEM grids (carbon-on-copper Quantifoil; Ted Pella). First, a PDMS film was transferred onto a clean glass substrate; then, TEM grid(s) were immobilized with the metal grid contacting the PDMS, exposing the carbon support for deposition. Bare glass substrates and glass-PDMS-grid substrate stacks were immediately transferred to an N_2-filled glovebox for deposition.

Illumination and plunge-freeze

The sample was mounted on a piston connected with compressed gas, as indicated in the supplemental information. A 405-nm UV LED was used for illumination with an intensity of 0.4 W/cm^2. The illumination time ranged from a half a minute to more than 8 min. After the desired illumination time, a valve was opened, allowing high-pressure-compressed gas to quickly inject the sample into a liquid nitrogen container to freeze the sample. The operations afterward were at cryogenic temperature, either in liquid nitrogen or in vacuum to avoid the influence of moisture or ice. Further details and a diagram of the setup are included in the supplemental information.

Cryogenic-STEM based characterization

ADF imaging, EELS mapping, and 4D-STEM were performed with an FEI 80-300 kV environmental transmission electron microscope (ETEM) at 300 kV. The $CsPb(Br_xI_{1-x})_3$ sample on TEM grids operated by illumination was transferred to Gatan 636

single-tilt liquid nitrogen cryo-transfer holder under liquid nitrogen. The sample was kept at $T = 98$ K through the whole process of characterization. Firstly, the morphology image was obtained with the ADF detector. Then, EELS mapping and 4D-STEM were measured correlatedly at the same area/grain. Then, the 4D-STEM measurement was taken at a low dose rate of ca. 4e/A^{2}s as measured from the fluorescent screen, with an exposure time of 0.04 s for each pixel. The diffraction pattern for each pixel was extracted to show the crystal orientation. In these diffraction patterns, the positions of each diffraction peak, as well as the zero-order peak, were fitted with Gaussian function. The lattice-parameter mapping was achieved by averaging the corresponding {100} plane spacing and calculating ($d_{hkl} = \frac{a}{\sqrt{h^2+k^2+l^2}}$) the lattice parameter at each pixel. Then, the same area was scanned again with the EELS detector with an electron dose of <20 e/A^{2}s and an exposure time of 0.5 s to avoid damage. The EELS detector measured the electron counts at a range of 569–1,081 eV, covering the range of the M5 peak for iodine at 619 nm and the M4 peak for cesium at 726 nm. The integral over the EELS peak calculated the areal atomic density of I and Cs at each pixel of scanning, which clearly showed the thickness variation separately and was used for calculating the I/Cs ratio.

RESOURCE AVAILABILITY

Lead contact

Requests for further information and resources should be directed to and will be fulfilled by the lead contact, Aaron M. Lindenberg (aaronl@stanford.edu).

Materials availability

All materials generated in this study are available from the lead contact with a completed materials transfer agreement.

Data and code availability

- Cryo-EM data from this work are available at the following repositories: EELS data, https://doi.org/10.5281/zenodo.15381626 and 4D-STEM data, https://doi.org/10.5281/zenodo.15381634.
- This paper does not report original code.
- Any additional information required to reanalyze the data reported in this paper is available from the lead contact upon request.

ACKNOWLEDGMENTS

This work was primarily supported by Exxon Mobil through its membership in the Stanford Strategic Energy Alliance. Yi Cui (author 9) acknowledges cryo-EM technique development support from the US Department of Energy, Office of Basic Energy Sciences, Division of Materials Sciences and Engineering, under contract DE-AC02-76SF00515. J.A.V. acknowledges fellowship support from the Stanford University Office of the Vice Provost of Graduate Education and the NSF Graduate Research Fellowship Program under grant no. DGE-1656518. Q.F. and A.M.L. acknowledge additional support for the PL measurements from the US Department of Energy, Office of Basic Energy Sciences, Division of Materials Sciences and Engineering, under contract DE-AC02-76SF00515.

AUTHOR CONTRIBUTIONS

A.M.L., H.I.K., and Yi Cui (author 9) conceived the idea. J.A.V. and Z.J. synthesized the perovskite samples and collected XRD measurements. Q.F., Yi Cui (author 2), and Y.L. performed the optical operations and plunge freezing of samples, as well as the cryogenic microscopic characterizations. Y.L. conducted the TEM imaging analysis. C.Z. helped with the cryogenic operations of the samples. Q.F. conducted the analysis of the EELS and 4D-STEM results. Q.F., Yi Cui (author 2), and Z.J. co-wrote the original manuscript. All authors discussed the results and commented on the manuscript.

DECLARATION OF INTERESTS

The authors declare no conflicts of interest.

SUPPLEMENTAL INFORMATION

Supplemental information can be found online at https://doi.org/10.1016/j.xcrp.2025.102653.

Received: November 24, 2024
Revised: April 7, 2025
Accepted: May 20, 2025
Published: June 11, 2025

REFERENCES

1. Stranks, S.D., Eperon, G.E., Grancini, G., Menelaou, C., Alcocer, M.J.P., Leijtens, T., Herz, L.M., Petrozza, A., and Snaith, H.J. (2013). Electron-hole diffusion lengths exceeding 1 micrometer in an organometal trihalide perovskite absorber. Science *342*, 341–344. https://doi.org/10.1126/science.1243982.
2. DeQuilettes, D.W., Vorpahl, S.M., Stranks, S.D., Nagaoka, H., Eperon, G.E., Ziffer, M.E., Snaith, H.J., and Ginger, D.S. (2015). Impact of microstructure on local carrier lifetime in perovskite solar cells. Science *348*, 683–686. https://doi.org/10.1126/science.aaa5333.
3. Green, M.A., Ho-Baillie, A., and Snaith, H.J. (2014). The emergence of perovskite solar cells. Nat. Photonics *8*, 506–514. https://doi.org/10.1038/NPHOTON.2014.134.
4. Kojima, A., Teshima, K., Miyasaka, T., and Shirai, Y. (2006). Novel photoelectrochemical cell with mesoscopic electrodes sensitized by lead-halide compounds. Meet. Abstr. *27*, 397. https://doi.org/10.1149/MA2006-02/7/397.
5. Eperon, G.E., Hörantner, M.T., and Snaith, H.J. (2017). Metal halide perovskite tandem and multiple-junction photovoltaics. Nat. Rev. Chem *1*, 0095. https://doi.org/10.1038/s41570-017-0095.
6. Noh, J.H., Im, S.H., Heo, J.H., Mandal, T.N., and Seok, S.I. (2013). Chemical management for colorful, efficient, and stable inorganic–organic hybrid nanostructured solar cells. Nano Lett. *13*, 1764–1769. https://doi.org/10.1021/nl400349b.
7. Fu, Y., Zhu, H., Chen, J., Hautzinger, M.P., Zhu, X.-Y., and Jin, S. (2019). Metal halide perovskite nanostructures for optoelectronic applications and the study of physical properties. Nat. Rev. Mater. *4*, 169–188. https://doi.org/10.1038/s41578-019-0080-9.
8. Wang, Y., Quintana, X., Kim, J., Guan, X., Hu, L., Lin, C.-H., Jones, B.T., Chen, W., Wen, X., Gao, H., and Wu, T. (2020). Phase segregation in inorganic mixed-halide perovskites: from phenomena to mechanisms. Photon. Res. *8*, A56–A80. https://doi.org/10.1364/PRJ.402411.
9. Slotcavage, D.J., Karunadasa, H.I., and McGehee, M.D. (2016). Light-Induced Phase Segregation in Halide-Perovskite Absorbers. ACS Energy Lett. *1*, 1199–1205. https://doi.org/10.1021/acsenergylett.6b00495.
10. Brennan, M.C., Ruth, A., Kamat, P.V., and Kuno, M. (2020). Photoinduced Anion Segregation in Mixed Halide Perovskites. Trends Chem. *2*, 282–301. https://doi.org/10.1016/j.trechm.2020.01.010.
11. Mahesh, S., Ball, J.M., Oliver, R.D.J., McMeekin, D.P., Nayak, P.K., Johnston, M.B., and Snaith, H.J. (2020). Revealing the origin of voltage loss in mixed-halide perovskite solar cells. Energy Environ. Sci. *13*, 258–267. https://doi.org/10.1039/C9EE02162K.
12. Hoke, E.T., Slotcavage, D.J., Dohner, E.R., Bowring, A.R., Karunadasa, H.I., and McGehee, M.D. (2015). Reversible photo-induced trap formation in

mixed-halide hybrid perovskites for photovoltaics. Chem. Sci. *6*, 613–617. https://doi.org/10.1039/C4SC03141E.

13. Mao, W., Hall, C.R., Chesman, A.S.R., Forsyth, C., Cheng, Y.-B., Duffy, N. W., Smith, T.A., and Bach, U. (2019). Visualizing phase segregation in mixed-halide perovskite single crystals. Angew. Chem. Int. Ed. *58*, 2893–2898. https://doi.org/10.1002/anie.201810193.
14. Brivio, F., Caetano, C., and Walsh, A. (2016). Thermodynamic origin of photoinstability in the $CH_3NH_3Pb(I_{1-x}Br_x)_3$ hybrid halide perovskite alloy. J. Phys. Chem. Lett. *7*, 1083–1087. https://doi.org/10.1021/acs.jpclett.6b00226.
15. Bischak, C.G., Hetherington, C.L., Wu, H., Aloni, S., Ogletree, D.F., Limmer, D.T., and Ginsberg, N.S. (2017). Origin of reversible photoinduced phase separation in hybrid perovskites. Nano Lett. *17*, 1028–1033.
16. Draguta, S., Sharia, O., Yoon, S.J., Brennan, M.C., Morozov, Y.V., Manser, J. S., Kamat, P.V., Schneider, W.F., and Kuno, M. (2017). Rationalizing the light-induced phase separation of mixed halide organic–inorganic perovskites. Nat. Commun. *8*, 200. https://doi.org/10.1038/s41467-017-02224-6.
17. Li, W., Rothmann, M.U., Liu, A., Wang, Z., Zhang, Y., Pascoe, A.R., Lu, J., Jiang, L., Chen, Y., Huang, F., et al. (2017). Phase segregation enhanced ion movement in efficient inorganic CsPbIBr2 solar cells. Adv. Energy Mater. *7*, 1700946. https://doi.org/10.1002/aenm.201700946.
18. Chen, W., Mao, W., Bach, U., Jia, B., and Wen, X. (2019). Tracking dynamic phase segregation in mixed-halide perovskite single crystals under two-photon scanning laser illumination. Small Methods *3*, 1900273. https://doi.org/10.1002/smtd.201900273.
19. Mao, W., Hall, C.R., Bernardi, S., Cheng, Y.-B., Widmer-Cooper, A., Smith, T.A., and Bach, U. (2021). Light-induced reversal of ion segregation in mixed-halide perovskites. Nat. Mater. *20*, 55–61. https://doi.org/10.1038/s41563-020-00826-y.
20. Tang, X., van den Berg, M., Gu, E., Horneber, A., Matt, G.J., Osvet, A., Meixner, A.J., Zhang, D., and Brabec, C.J. (2018). Local observation of phase segregation in mixed-halide perovskite. Nano Lett. *18*, 2172–2178. https://doi.org/10.1021/acs.nanolett.8b00505.
21. Luo, Y., Zhang, S., Chen, J.S., Ma, X., Ma, K., Deng, J., Jiang, Y., Li, L., Lai, B., Chen, S., et al. (2023). Photo-induced halide redistribution in 2D halide perovskite lateral heterostructures. Joule *7*, 2376–2385. https://doi.org/10.1016/j.joule.2023.08.003.
22. Lee, H., Boonmongkolras, P., Jun, S., Kim, D., Park, Y., Koh, J., Cho, Y.-H., Shin, B., and Park, J.Y. (2023). In situ observation of photoinduced halide segregation in mixed halide perovskite. ACS Appl. Energy Mater. *6*, 1565–1574. https://doi.org/10.1021/acsami.9b06418.
23. Peng, S., Wang, Y., Braun, M., Yin, Y., Meng, A.C., Tan, W., Saini, B., Severson, K., Marshall, A.F., Sytwu, K., et al. (2023). Kinetics and mechanism of light-induced phase separation in a mixed-halide perovskite. Matter *6*, 2052–2065. https://doi.org/10.1016/j.matt.2023.04.025.
24. Suchan, K., Merdasa, A., Rehermann, C., Unger, E.L., and Scheblykin, I.G. (2020). Complex evolution of photoluminescence during phase segregation of $MAPb(I_{1-x}Br_x)_3$ mixed halide perovskite. J. Lumin. *221*, 117073. https://doi.org/10.1016/j.jlumin.2020.117073.
25. Caprioglio, P., Caicedo-Dávila, S., Yang, T.C.-J., Wolff, C.M., Peña-Camargo, F., Fiala, P., Rech, B., Ballif, C., Abou-Ras, D., Stolterfoht, M., et al. (2021). Nano-emitting heterostructures violate optical reciprocity and enable efficient photoluminescence in halide-segregated methylammonium-free wide bandgap perovskites. ACS Energy Lett. *6*, 419–428. https://doi.org/10.1021/acsenergylett.0c02270.
26. Li, Y., Zhou, W., Li, Y., Huang, W., Zhang, Z., Chen, G., Wang, H., Wu, G.-H., Rolston, N., Vila, R., et al. (2019). Unravelling degradation mechanisms and atomic structure of organic-inorganic halide perovskites by cryo-EM. Joule *3*, 2854–2866. https://doi.org/10.1016/j.joule.2019.08.016.
27. Divitini, G., Cacovich, S., Matteocci, F., Cinà, L., Di Carlo, A., Ducati, C., and Ducati, C. (2016). In situ observation of heat-induced degradation of perovskite solar cells. Nat. Energy *1*, 15012. https://doi.org/10.1038/nenergy.2015.12.
28. Woodward, P.M. (1997). Octahedral Tilting in Perovskites. II. Structure Stabilizing Forces. Acta Crystallogr. B *53*, 44–66. https://doi.org/10.1107/S0108768196012050.
29. Sharma, S., Weiden, N., and Weiss, A. (1992). Phase Diagrams of Quasi-binary Systems of the Type: ABX3 — A′BX3; ABX3 — AB′X3, and ABX3 — ABX′3; X = Halogen. Zeitschrift für Physikalische Chemie *175*, 63–80.
30. Beal, R.E., Slotcavage, D.J., Leijtens, T., Bowring, A.R., Belisle, R.A., Nguyen, W.H., Burkhard, G.F., Hoke, E.T., and McGehee, M.D. (2016). Cesium Lead Halide Perovskites with Improved Stability for Tandem Solar Cells. J. Phys. Chem. Lett. *7*, 746–751. https://doi.org/10.1021/acs.jpclett.6b00002.
31. Beal, R.E., Slotcavage, D.J., Leijtens, T., Bowring, A.R., Belisle, R.A., Nguyen, W.H., Burkhard, G.F., Hoke, E.T., and McGehee, M.D. (2016). Cesium lead halide perovskites with improved stability for tandem solar cells. J. Phys. Chem. Lett. *7*, 746–751. https://doi.org/10.1021/acs.jpclett.6b00002.
32. Sutton, R.J., Eperon, G.E., Miranda, L., Parrott, E.S., Kamino, B.A., Patel, J.B., Hörantner, M.T., Johnston, M.B., Haghighirad, A.A., Moore, D.T., and Snaith, H.J. (2016). Bandgap-tunable cesium lead halide perovskites with high thermal stability for efficient solar cells. Adv. Energy Mater. *6*, 1502458. https://doi.org/10.1002/aenm.201502458.
33. Ophus, C. (2019). Four-dimensional scanning transmission electron microscopy (4D-STEM): From scanning nanodiffraction to ptychography and beyond. Microsc. Microanal. *25*, 563–582. https://doi.org/10.1017/S1431927619000497.
34. Zhao, Y., Miao, P., Elia, J., Hu, H., Wang, X., Heumueller, T., Hou, Y., Matt, G.J., Osvet, A., Chen, Y.-T., et al. (2020). Strain-activated light-induced halide segregation in mixed-halide perovskite solids. Nat. Commun. *11*, 6328. https://doi.org/10.1038/s41467-020-20066-7.
35. Brennan, M.C., Draguta, S., Kamat, P.V., and Kuno, M. (2018). Light-induced anion phase segregation in mixed halide perovskites. ACS Energy Lett. *3*, 204–213. https://doi.org/10.1021/acsenergylett.7b01151.
36. Limmer, D.T., and Ginsberg, N.S. (2020). Photoinduced phase separation in the lead halides is a polaronic effect. J. Chem. Phys. *152*, 230901. https://doi.org/10.1063/1.5144291.